Spatially Adaptive Superresolution Land Cover Mapping With Multispectral and Panchromatic Images

Xiaodong Li, Feng Ling, Yun Du, and Yihang Zhang

Abstract—Superresolution land cover mapping (SRM) is a technique for generating land cover maps with a finer spatial resolution than the input image. In general, either the original multispectral (MS) images or the spectral unmixing results of the MS image are used as input for SRM models. Panchromatic (PAN) images are often captured together with MS images by many remote sensors and provide more spatial information due to their higher spatial resolution compared with the MS image. In this paper, a spatially adaptive spatial–spectral managed SRM model (SA_SSMSRM) that incorporates both MS and PAN images is proposed. SA_SSMSRM aims to better smooth homogeneous regions of objects (which represent a territory within which there is a uniformity in terms of land cover class) and preserve land cover class boundaries simultaneously by using the PAN image pixel photometric distance (i.e., gray-level distance or pixel value difference). Homogeneous regions in the PAN images are usually characterized by the photometric (pixel value) similarity, whereas class boundaries are usually characterized by photometric dissimilarity. The SA_SSMSRM smoothing parameter, which controls the contribution of the prior term (which encodes prior knowledge about land cover spatial patterns), is designed to be spatially adaptive, with its value decreasing if the photometric similarity of neighboring PAN image pixels decreases. SA_SSMSRM was examined on high-spatial-resolution QuickBird images, IKONOS images, and Advanced Land Observing Satellite (ALOS) images with both MS and PAN data. Results showed that the proposed SA_SSMSRM can generate more accurate superresolution maps than other SRM models.

Index Terms—Panchromatic (PAN) image, photometric distance, smoothing parameter, spatially adaptive, superresolution land cover mapping (SRM).

I. INTRODUCTION

SUPERRESOLUTION land cover mapping (SRM) (or subpixel land cover mapping) is a technique used for generating land cover maps with a finer spatial resolution than the input data [1], [2]. This technique has been used for land cover mapping [3], [4], waterline mapping [5], [6], urban building mapping [7], urban tree mapping [8], subpixel-scale land cover change mapping [9], and the improvement of landscape pattern index accuracy [10]. One type of SRM algorithms (including the pixel swapping algorithm (PSA) [10]–[12], Hopfield neural networks [3], [13], [14], linear optimization [15], spatial attraction model [16]–[19], genetic algorithm [20], particle swarm optimization [21], and interpolation-based SRM [22]) uses fraction images (which are the result of the spectral unmixing of a multispectral (MS) image) as the input. Another type of SRM algorithms (called spatial–spectral managed SRM (SSM-SRM) and including Markov-random-field-based SRM [23], [24], SRM with constrained linear spectral unmixing (CLSU) model [25], and supervised fuzzy c-means based SRM [26]) does not use fraction images as the input and can be applied directly to remotely sensed images [23]–[26].

The MS image pixels are inputted directly or indirectly (the indirect input is the fraction images which are generated by spectral unmixing and indicate the proportions of each land cover class within each pixel) into an SRM model. SRM is formulated as an ill-posed problem that reconstructs a fine-spatial-resolution land cover map from an MS image or a set of class fraction images with a coarse spatial resolution, and the SRM has a limit to the spatial detail and accuracy of the resultant superresolution (SR) land cover map. An effective way to improve the SRM accuracy is using ancillary data in addition to the MS image. The ancillary data used for an SRM include the digital elevation model (DEM) [6], vector boundaries [27], multiple subpixel shifted remotely sensed images [13], and light detection and ranging (LIDAR) data [28].

Among the several MS remote sensors such as the Quick-Bird, IKONOS, Satellite pour l'Observation de la Terre (SPOT)-5, and Landsat Enhanced Thematic Mapper Plus, a panchromatic (PAN) and an MS image are often captured together. The PAN image provides more spatial information due to its higher spatial resolution compared with the MS image. The PAN image can be utilized to identify homogeneous regions of objects which represent a territory within which there is a uniformity in terms of land cover class and class boundaries [29], [30]. In a PAN image, homogeneous regions are characterized by photometric similarity, and class boundaries are characterized by photometric dissimilarity. However, in previous studies, many SRM models (such as the Hopfield neural network-based SRM [31], [32] and Markov-random-field-based SRM [8]) only used the PAN image as the spectral

constraint to preserve the observed pixel spectrums in the synthetic image pixels created by an SR land cover map, and the information of the photometric similarity of neighboring PAN image pixels was not utilized.

In this paper, an SSMSRM model that incorporates both MS and PAN images is proposed. SSMSRM can be applied directly to the remotely sensed images. The proposed SSMSRM contains three parts: a prior term (or spatial term), a spectral term, and a smoothing parameter. The prior term encodes prior knowledge about land cover spatial patterns. The spectral term aims to minimize the difference in the spectral value between the synthetic MS (or PAN) image pixels and the observed MS (or PAN) image pixels. The smoothing parameter is used to control the contribution of the prior term.

The appropriate setting of the smoothing parameter is essential to generate the SR map with high accuracy. Generally, SSMSRM adopts a fixed smoothing parameter regardless that a subpixel is on a class boundary or within a homogeneous region. When a subpixel is located in a homogeneous region, a high value of the smoothing parameter should be applied to remove speckle artifacts. When a subpixel is located on the class boundary, a low value of the smoothing parameter should be applied to avoid oversmoothing. In this paper, a spatially adaptive smoothing parameter in SSMSRM is assigned to smooth the homogeneous region and preserve the class boundary simultaneously. A photometric distance (i.e., gray-level distance or pixel value difference) decay function is designed to decrease the smoothing parameter values for subpixels whose corresponding PAN image pixel values are dissimilar so that SSMSRM can simultaneously smooth the homogeneous regions and preserve class boundaries in an SR map.

For SSMSRM with a fixed smoothing parameter, the optimal smoothing parameter is often obtained experimentally using a set of trials on a land cover image, and this process is time consuming [25], [26]. There are theoretical methods for searching the optimal fixed value or spatially adaptive values for the smoothing parameter in Markov-random-field-based SRM [24], [33]. However, these methods are based on the energy balance analysis theory and thus complex. A simple method to optimize the smoothing parameter is desired. The optimization of the smoothing parameter in SSMSRM is affected by the data ranges of both prior and spectral terms [34]. In order to alleviate the effects of data ranges on the optimization of the smoothing parameter, the prior and spectral terms are divided by two adaptive coefficients which are calculated according to the statistical characters of the data ranges of both terms. This approach can simplify the process of optimization of the spatially adaptive smoothing parameter in SSMSRM.

In this paper, a spatially adaptive SSMSRM (SA_SSMSRM) model was proposed and was performed on high-spatial-resolution QuickBird images, IKONOS images, and ALOS images with both MS and PAN data. The remainder of this paper is organized as follows. Section II introduces the SSMSRM model. The SA_SSMSRM model is developed in Section III. Section IV presents the model optimization. Section V examines the performance of SA_SSMSRM against other SRM models. Conclusions are provided in Section VI.

II. SSMSRM MODEL

A. SSMSRM Model Objective Function

Suppose that the MS image is $\mathbf{Y}$ with spatial resolution $R_{\mathbf{Y}}$ and $\mathbf{Y}$ contains b bands, with each band containing N pixels. The PAN image is $\mathbf{Z}$ with spatial resolution $R_{\mathbf{Z}}$. The output of SRM is an SR land cover map $\mathbf{X}$ with spatial resolution $R_{\mathbf{X}}$, and the SR map contains c land cover classes. The scale factor, which allows to generate land cover maps of different spatial resolutions for a given input image, is an input parameter of SRM. The scale factor between an MS pixel and a subpixel is defined as $F_{\mathbf{YX}}$ ($F_{\mathbf{YX}} = R_{\mathbf{Y}}/R_{\mathbf{X}}$), and each MS pixel is divided into $F_{\mathbf{YX}}^2$ subpixels. The scale factor between a PAN pixel and a subpixel is defined as $F_{\mathbf{ZX}}$ ($F_{\mathbf{ZX}} = R_{\mathbf{Z}}/R_{\mathbf{X}}$), and each PAN pixel is divided into $F_{\mathbf{ZX}}^2$ subpixels.

The SSMSRM objective function E is written as [25]

$$E = \lambda \cdot E^p + E^s \tag{1}$$

where E^p is the prior term that encodes prior knowledge about land cover spatial patterns; E^s is the spectral term and the pixel matching term, and it is used to describe the degree of match between the observed image pixel spectrums and the synthetic image pixel spectrums created by an SR land cover map. λ is the smoothing parameter that controls the contribution of E^p.

B. Prior Term

Prior term E^p in SSMSRM is used to describe the degree of match between the SR land cover map and a prior spatial pattern model. Based on the assumption that spatially proximate observations of a given property are more similar than that of more distant observations, the goal of SRM is to maximize the spatial correlation of neighboring subpixels in this paper [2], [12], [15]. The prior term for the subpixel k in MS pixel i, called $a_{i,k}$, is computed as

$$E^p\left(c(a_{i,k})\right) = \sum_{l \in N(a_{i,k})} w(a_{i,k}, a_l) \cdot \delta\left(c(a_{i,k}), c(a_l)\right). \tag{2}$$

$N(a_{i,k})$ is a symmetric neighborhood that includes all subpixels inside a square window (the window size, which is the length of the square side of the neighborhood, is W) whose center is $a_{i,k}$ ($a_{i,k}$ itself is not included in the window). $c(a_{i,k})$ and $c(a_l)$ are the land cover class labels for subpixel $a_{i,k}$ and subpixel a_l ($l \in N(a_{i,k})$). $\delta(c(a_{i,k}), c(a_l))$ is defined as

$$\delta\left(c(a_{i,k}), c(a_l)\right) = \begin{cases} -1 & c(a_l) = c(a_{i,k}) \\ 0 & c(a_l) \neq c(a_{i,k}). \end{cases} \tag{3}$$

The prior term prefers a solution of SRM that reduces the occurrence of subpixels with different class labels in $N(a_{i,k})$. $w(a_{i,k}, a_l)$ is the weight for a neighborhood subpixel a_l calculated through a geometric distance decay function [35] and is often set to be inversely proportional to the geometric distance $d_g(a_{i,k}, a_l)$ (usually the Euclidean distance that characterizes the spatial closeness of subpixels) between $a_{i,k}$ and a_l [8]

$$w(a_{i,k}, a_l) = \frac{1}{d_g(a_{i,k}, a_l)}. \tag{4}$$

C. Spectral Term

It is intended that the SSMSRM model can be directly applied to remotely sensed images [2], [23], [25], [26]. The spectral term E^s aims to match the observed pixel spectrums in the synthetic image pixels created by the SR land cover map. E^s can be obtained by a variety of methods, including the Gaussian maximal likelihood method [8], [23], [24], [33], the least square error method [25], and the fuzzy c-means method [26]. In this paper, the least square error method was utilized, which aims to minimize the spectral value difference between the synthetic pixels and the observed pixels based on the least square error. Unlike the reported least square error method that only includes the data from MS images in E^s [25], the proposed method incorporates the data from both MS and PAN images in E^s.

Let $\boldsymbol{\mu}_i$ be a $b \times 1$ synthetic coarse pixel column vector of image $\mathbf{Y}$. Assume $\mathbf{S}_{MS}$ to be the MS signature matrix

$$\mathbf{S}_{MS} = \begin{bmatrix} S_{MS(B1,C1)} & \cdots & S_{MS(B1,Cc)} \\ S_{MS(B2,C1)} & \cdots & S_{MS(B2,Cc)} \\ \cdots & \cdots & \cdots \\ S_{MS(Bb,C1)} & \cdots & S_{MS(Bb,Cc)} \end{bmatrix} \quad (5)$$

where $S_{MS(Bb,Cc)}$ denotes the spectral signature of the cth land cover class in the bth band in the MS image. Assume that $\boldsymbol{P}_{MS,i} = (P_1, P_2, \ldots, P_c)^T$ (where T denotes the vector transposition) is a $c \times 1$ abundance column vector associated with $\boldsymbol{\mu}_i$, where $P_1, P_2, \ldots, P_c$ represents the abundances of land cover classes in $\boldsymbol{\mu}_i$. Assuming that the spectra of subpixels are linearly combined, the synthetic MS pixel vector $\boldsymbol{\mu}_i$ can be expressed as

$$\boldsymbol{\mu}_i = \mathbf{S}_{MS} \times \boldsymbol{P}_{MS,i}. \quad (6)$$

Assume that the observed MS pixel vector is $\boldsymbol{y}_i$. Using the least square error to describe the spectral value difference [25], the MS spectral term E^s_{MS} for the subpixel $a_{i,k}$ is then written as

$$E^s_{MS}(c(a_{i,k})) = (\boldsymbol{y}_i - \boldsymbol{\mu}_i)^T (\boldsymbol{y}_i - \boldsymbol{\mu}_i). \quad (7)$$

Likewise, the synthetic PAN pixel value v_j is expressed as

$$v_j = \boldsymbol{S}_{PAN} \times \boldsymbol{P}_{PAN,j} \quad (8)$$

where $\boldsymbol{P}_{PAN,j}$ is a $c \times 1$ abundance column vector associated with v_j and $\boldsymbol{S}_{PAN}$ is the PAN spectral signature vector formulated as

$$\boldsymbol{S}_{PAN} = [S_{PAN(C1)}, \ldots, S_{PAN(Cc)}] \quad (9)$$

where $S_{PAN(Cc)}$ denotes the spectral signature of the cth land cover class in the PAN image. Assume that the observed PAN pixel value is z_j. The PAN spectral term E^s_{PAN} for the subpixel $a_{j,k}$ is written as

$$E^s_{PAN}(c(a_{j,k})) = (z_j - v_j)^2. \quad (10)$$

Based on (7) and (10), the spectral term for the subpixel $a_{i,k}$ is written as

$$E^s(c(a_{i,k})) = E^s_{MS}(c(a_{i,k})) + E^s_{PAN}(c(a_{j,k})). \quad (11)$$

III. SA_SSMSRM

A. Determination of Spatially Adaptive Smoothing Parameter

Using a fixed smoothing parameter usually promotes solutions in which adjacent pixels are likely to belong to the same class in spatial–spectral managed image classification and segmentation [36], [37]. Similarly, SSMSRM with a fixed smoothing parameter promotes SR maps with smooth spatial patterns. For SSMSRM, on the one hand, a high value of the smoothing parameter is required to remove speckle artifacts and generate high-accuracy homogeneous regions in the SR map. On the other hand, a low value of the smoothing parameter is required to preserve land cover class boundaries. In the PAN image, homogeneous regions are usually characterized by photometric similarity, and class boundaries are usually characterized by photometric dissimilarity. The photometric distance between PAN pixels, which characterizes the similarity of the corresponding neighboring subpixel resembling the central subpixel, is utilized to set appropriate smoothing parameter values for different neighboring subpixels.

As each PAN image pixel is divided into several subpixels according to the scale factor, the similarity of subpixels, which are located in the same PAN pixel, cannot be distinguished by the PAN pixel value. The PAN image pixels need to be processed to the subpixel scale so that the spatial resolution of the PAN image matches the fine-resolution land cover map. Numerous interpolation algorithms can be applied for this purpose. In this paper, three algorithms (nearest-neighbor interpolation, bilinear interpolation, and bicubic interpolation) are tried. In the nearest-neighbor interpolation, the nearby PAN pixel values are used as the interpolated PAN pixel values. In bilinear and bicubic interpolations, the average of 4 (2×2) surrounding PAN pixel values and the average of 16 (4×4) surrounding PAN pixel values are used for the interpolated PAN pixel values [38]. The nearest-neighbor interpolated images are discontinuous in gray values, whereas the bilinear and bicubic interpolated images are often smoother and have fewer interpolation artifacts.

One assumption on the spatially adaptive smoothing parameter is that smaller photometric distance (similar pixel value) between interpolated PAN pixels indicates higher probability of the subpixel labels being in homogeneous regions and larger photometric distance (dissimilar pixel value) between interpolated PAN pixels indicates higher probability of the subpixel labels being on class boundaries. Assume that $g(a_{i,k})$ and $g(a_l)$ are the pixel values in the interpolated PAN image corresponding to subpixels $a_{i,k}$ and a_l. $d_p(g(a_{i,k}), g(a_l))$ is the photometric distance between $g(a_{i,k})$ and $g(a_l)$ and can be set as the absolute difference of the interpolated PAN pixel values ($|g(a_{i,k}) - g(a_l)|$). For a smaller value of $d_p(g(a_{i,k}), g(a_l))$, a_l needs to be assigned with the same class label as $c(a_{i,k})$ to smooth the region allocated by a_l and $a_{i,k}$ in the SRM. In contrast, for a larger value of $d_p(g(a_{i,k}), g(a_l))$, a_l needs to be assigned with a class label different from $c(a_{i,k})$ to reconstruct the class boundary in the region allocated by a_l and $a_{i,k}$.

In this paper, the spatially adaptive smoothing parameter λ^* is introduced, and the Gaussian photometric distance decay function is used to measure the smoothing parameter
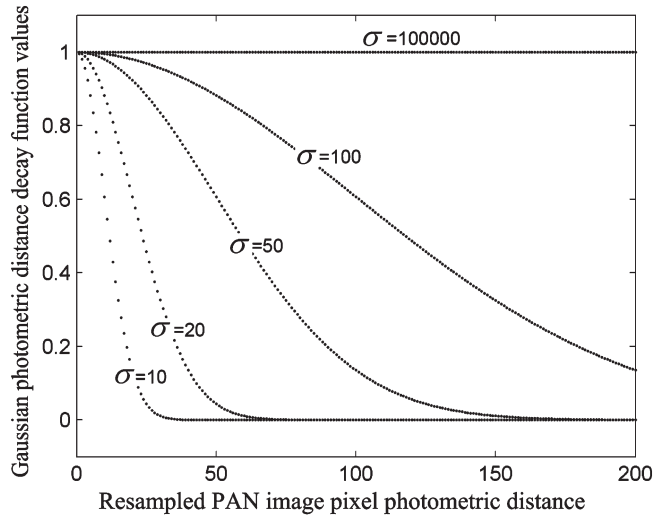
Fig. 1. Curves of the Gaussian photometric distance decay function values against the nonlinear parameter σ in SA_SSMSRM.
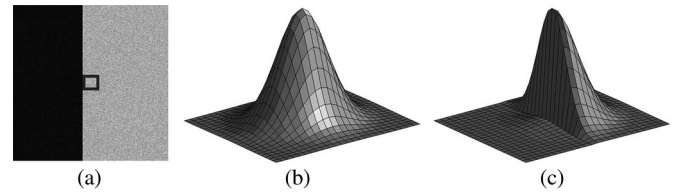

Fig. 2. (a) Central subpixel (in the square frame) in the interpolated PAN image. (b) Combined weights for the neighborhoods with centered target subpixel in SSMSRM with a fixed smoothing parameter. (c) Combined weights for the neighborhoods with centered target subpixel in SA_SSMSRM.

value $\lambda^*(a_{i,k}, a_l)$ based on the photometric distance $d_p(g(a_{i,k}), g(a_l))$

$$\lambda^*(a_{i,k}, a_l) = \lambda_0 \cdot e^{-0.5 \cdot (d_p(g(a_{i,k}), g(a_l))/\sigma)^2} \quad (12)$$

where λ_0 is the smoothing parameter value in the case that the interpolated PAN image pixel value of a subpixel equals to that of the central subpixel. σ is a nonlinear parameter.

Fig. 1 shows the curves of the Gaussian photometric distance decay function values against the nonlinear parameter σ in SA_SSMSRM. When σ is small, the smoothing parameters for the subpixels associated with larger interpolated PAN pixel photometric distances decrease drastically. When σ is high, the smoothing parameters for the subpixels associated with different interpolated PAN pixel photometric distances are approximate. For an extremely large value of σ, the smoothing parameters for all subpixels are almost equal, and SA_SSMSRM and SSMSRM which uses a fixed smoothing parameter will produce similar SR maps.

The prior term and the smoothing parameter are multiplied to play a combined role in the labeling of subpixels in SSMSRM, according to (1). Fig. 2 shows the combined weights of the prior term and the smoothing parameter for subpixels in a neighborhood system in an ordinary SSMSRM (O_SSMSRM) with a fixed smoothing parameter and SA_SSMSRM, according to

O_SSMSRM : $\lambda \cdot E^p(c(a_{i,k}))$

$$= \lambda \cdot \sum_{l \in N(a_{i,k})} \frac{\delta(c(a_{i,k}), c(a_l))}{d_g(a_{i,k}, a_l)} \quad (13)$$

SA_SSMSRM : $\lambda^* \cdot E^p(c(a_{i,k}))$

$$= \lambda_0 \cdot \sum_{l \in N(a_{i,k})} e^{-0.5 \cdot (d_p(g(a_{i,k}), g(a_l))/\sigma)^2} \cdot \frac{\delta(c(a_{i,k}), c(a_l))}{d_g(a_{i,k}, a_l)}. \quad (14)$$

Fig. 2(a) shows that the target subpixel is located between class boundaries. For O_SSMSRM, the combined weights

for neighboring subpixels follow the geometric distance decay function measured by $1/d_g(a_{i,k}, a_l)$, indicating that the combined weights are suppressed as the geometric distance increases. The local variation of pixel values, an indicator of class boundaries in the PAN image, is ignored. Consequently, the class boundary may probably be smoothed in the finalized SR map. By contrast, the photometric similarity of the interpolated PAN image pixels is considered in SA_SSMSRM. The combined weights for the neighboring subpixels whose pixel values are dissimilar to that of the target subpixel are suppressed (14). In this way, the target subpixel is more likely to be labeled as a class similar to the subpixel labels located on the right side of Fig. 2(a), and more likely, the class boundaries can be preserved in the finalized SR map.

The adoption of the spatially adaptive smoothing parameter in SSMSRM is similar to the bilateral filtering used in image processing [39], [40]. SA_SSMSRM and the bilateral filtering have similar aims—to smooth homogeneous regions and preserve class boundaries. The difference is that bilateral filtering is used for generating gray or color images, whereas SA_SSMSRM is used for generating land cover maps. For bilateral filtering, the homogeneous region is represented as consecutive signal values in gray or color images. For SRM, the homogeneous region is represented as a territory within which there is a uniformity in terms of land cover class in thematic maps. In order to smooth the homogeneous regions and preserve class boundaries simultaneously, bilateral filtering uses a low-pass domain filter to average pixel values which occupy a nearby spatial location based on geometric distance and uses a range filter to average pixel values with weights that decay with photometric dissimilarity [39], [40]. By contrast, SA_SSMSRM uses a geometric distance decay function to reduce the weights for subpixels which are located spatially distant to the target subpixel and uses a photometric distance decay function to reduce the weights for subpixels whose corresponding PAN image pixel values are dissimilar to the PAN pixel value of the target subpixel.

B. Estimation of λ_0

Based on (1), (11), and (14), the SA_SSMSRM objective function for the subpixel $a_{i,k}$ is expressed as

$$E(c(a_{i,k})) = \lambda^* \cdot E^p(c(a_{i,k})) + E^s(c(a_{i,k}))$$

$$= \lambda_0 \cdot E^p_{SA}(c(a_{i,k})) + E^s(c(a_{i,k})) \quad (15)$$

where $E_{SA}^p(c(a_{i,k}))$ is the revised prior term according to the spatially adaptive smoothing parameter and is calculated as

$$E_{SA}^p\left(c\left(a_{i,k}\right)\right) = \sum_{l \in N(a_{i,k})} e^{-0.5 \cdot (d_p(g(a_{i,k}),g(a_l))/\sigma)^2}$$
$$\cdot \frac{\delta\left(c(a_{i,k}), c(a_l)\right)}{d_g\left(a_{i,k}, a_l\right)}. \quad (16)$$

Obviously, the accurate labeling of the subpixel $a_{i,k}$ depends on an appropriate setting of λ_0.

The data range of the prior term depends on the neighborhood window size, the geometric distance decay function of subpixels, and the photometric distance decay function of interpolated PAN image pixels. The data range of the spectral term also varies drastically depending on the number of land cover classes, the radiometric resolution of the input image, and the number of bands. The uncertainty associated with the data ranges of the prior and spectral terms hinders the optimization of the smoothing parameter. Jia and Richards [34] proposed a method to alleviate the influence of the date range of prior and spectral terms on spatial–spectral managed classification at the pixel scale. In this paper, transformations of the prior and spectral terms are performed at the subpixel scale to alleviate the influence of the data range of prior and spectral terms in SA_SSMSRM.

For each subpixel, the revised prior term is divided by the sum of the absolute values of all subpixels in all classes

$$E^p\left(c(a_{i,k})\right)^* = \frac{E_{SA}^p\left(c(a_{i,k})\right)}{\sum_{n=1}^{N} \sum_{m=1}^{F_{YX}^2} \sum_{\alpha=1}^{c} \left|E_{SA}^p\left(c_\alpha(a_{n,m})\right)\right|} \quad (17)$$

where $c_\alpha(a_{n,m})$ denotes the label of the αth class for subpixel $a_{n,m}$.

For each subpixel, the spectral term is divided by the sum of all subpixels in all classes

$$E^s\left(c(a_{i,k})\right)^* = \frac{E^s\left(c(a_{i,k})\right)}{\sum_{n=1}^{N} \sum_{m=1}^{F_{YX}^2} \sum_{\alpha=1}^{c} E^s\left(c_\alpha(a_{n,m})\right)}. \quad (18)$$

The SA_SSMSRM objective function is thus rewritten as

$$E\left(c(a_{i,k})\right) = \lambda_0 \cdot E^p\left(c(a_{i,k})\right)^* + E^s\left(c(a_{i,k})\right)^*. \quad (19)$$

The objective function in (19) is essentially a modification of (15) by dividing the prior and spectral terms by two adaptive coefficients. The SA_SSMSRM objective function can be solved by iterative methods such as iterative conditional modes and simulated annealing [41]. In each iteration, the two adaptive coefficient values are calculated first. Then, the prior and spectral terms for all subpixels are divided by these two adaptive coefficients which are fixed as constants in each iteration. In this way, the modification of the objective function does not change the decision rule. As the data ranges of both prior and spectral terms are considered in (19), it is easier to set the value of the smoothing parameter. The important mathematical variables are shown in Table I.

TABLE I
MATHEMATICAL VARIABLES DEFINITION

Variables	Definition
$\mathbf{X}$	Superresolution land cover map
$\mathbf{Y}$	MS image
$\mathbf{Z}$	PAN image
$\boldsymbol{y}_i$	Observed MS pixel vector of image $\mathbf{Y}$
$\boldsymbol{\mu}_i$	Synthetic MS pixel vector of image $\mathbf{Y}$
z_j	Observed PAN pixel value of image $\mathbf{Z}$
v_j	Synthetic PAN pixel value of image $\mathbf{Z}$
$\boldsymbol{P}_{MS,i}$	Abundance column vector associated with $\boldsymbol{\mu}_i$
$\boldsymbol{P}_{PAN,j}$	Abundance column vector associated with v_j
$R_{\mathbf{X}}$	Spatial resolution of $\mathbf{X}$
$F_{\mathbf{YX}}$	Scale factor between $\mathbf{Y}$ and $\mathbf{X}$
N	Number of coarse-resolution pixels in image $\mathbf{Y}$
W	Neighborhood window size of a target subpixel
b	Number of bands in image $\mathbf{Y}$
c	Number of land cover classes
$a_{i,k}$	Subpixel k in MS pixel i
$N(a_{i,k})$	Subpixels in a symmetric neighborhood with the center subpixel $a_{i,k}$
$c(a_{i,k})$	Class label of subpixel $a_{i,k}$
$g(a_{i,k})$	Pixel value of subpixel $a_{i,k}$ in the interpolated PAN image
$d_g\left(a_{i,k}, a_l\right)$	Geometric distance between $a_{i,k}$ and a_l
$d_p\left(g(a_{i,k}), g(a_l)\right)$	Photometric distance between $g(a_{i,k})$ and $g(a_l)$
λ_0	Smoothing parameter in SA_SSMSRM
σ	Nonlinear parameter in the photometric distance decay function

IV. MODEL OPTIMIZATION AND ACCURACY ASSESSMENT

A. Model Optimization

The initialized SR map affects the convergence speed of the model and the accuracy of the final SR map. In this paper, the initialized SR map is generated according to the fraction images generated from a spectral unmixing model. This initialization is widely used in SSMSRM to achieve fast convergence and high accuracy [10], [23], [24], [26]. The CLSU algorithm was applied to unmix the MS image [42]. The number of subpixels in each class and in each MS image pixels is determined by multiplying the class area proportion according to fraction images and the square of scale factor ($F_{\mathbf{YX}}^2$). Finally, the subpixels within each MS image pixel are randomly located, and the initialized SR map is obtained.

The generation of the optimal SR map by SA_SSMSRM is achieved by minimizing the objective function in (19). Simulated annealing is a widely used algorithm to solve single and multiobjective optimization problems where a desired global minimum is hidden among many local minima [41]. Simulated annealing can avoid being trapped in the local minimum by controlling the acceptance of some inferior solutions which increase the objective function's value [43]. The acceptance of inferior solutions is dependent on a parameter T, which
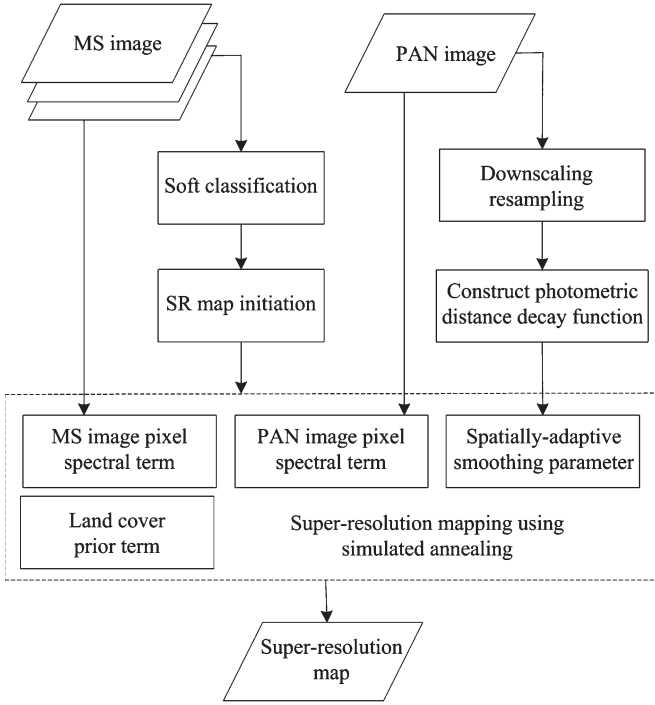
Fig. 3. Flow chart of the SA_SSMSRM model.

is analogous to the temperature associated with the physical processes of the annealing of molten model. The annealing algorithm is defined on a power law decay function, where T at iteration *count* is changed according to

$$T_{count} = \gamma \cdot T_{count-1}. \qquad (20)$$

The parameter $\gamma \in (0, 1)$ controls the rate of temperature decrease. With the decrement of T, the inferior solutions will be accepted with low probability, and simulated annealing terminates when T is very small where the global minimum of the objective function is reached. All subpixel labels are updated using the Metropolis–Hastings sampler [43]. The optimal values of the simulated annealing parameters play an important role in SSMSRM. For both O_SSMSRM and SA_SSMSRM, the optimal simulated annealing parameter values were set through many trials. In this paper, the initial temperature was set as 3, the maximal iteration number was set as 120, and the parameter γ was set as 0.9 [24]. With these simulated annealing parameters, the convergence of the model was reached between 70 and 120 iterations for all experiments. The entire SA_SSMSRM process is illustrated in Fig. 3.

Step 1) Unmix the MS image to generate fraction images, and initiate the SR land cover map.
Step 2) Interpolate the PAN image to the subpixel scale.
Step 3) Increase the iteration number and decrease the temperature. Calculate the adaptive coefficients for the prior and spectral terms according to (17) and (18). Update all the subpixel labels using the Metropolis–Hastings sampler [43].

Step 4) End the iteration if the iteration number reaches a predefined number or if less than 0.1% of the total subpixels were changed after two consecutive iterations. Otherwise, increase the iteration number, and return to Step 3).

B. Accuracy Assessment

The overall accuracy (OA), which is defined at the fine-resolution pixel scale (subpixel scale), was adopted to evaluate the accuracy of the model [44]. OA is defined as the ratio of the number of correctly labeled subpixels to the total number of subpixels in the image. The root-mean-square error of fraction images (fraction RMSE), which measures the difference in each MS pixel between the SR land cover map produced by SRM and the reference land cover map used for validation, was also applied [45]

$$\text{fraction RMSE} = \frac{1}{c} \sum_{\alpha=1}^{c} \sqrt{\frac{1}{N} \sum_{i=1}^{N} (\theta_{\alpha i} - \omega_{\alpha i})^2} \qquad (21)$$

where $\theta_{\alpha i}$ is the class area proportion of class α in the MS pixel i in the SR land cover map and $\omega_{\alpha i}$ is the class area proportion of class α in the MS pixel i in the reference land cover map. In addition, the mean square error (MSE) was used to evaluate the gray-level similarity between the origin fine-resolution PAN image (which is used for manually digitalizing the reference map) and the interpolated fine-resolution PAN image produced by the nearest-neighbor, bilinear, and bicubic interpolations from the coarse-resolution PAN image (which is used as SA_SSMSRM input). MSE is calculated as

$$\text{MSE} = \frac{1}{N \times F_{YX}^2} \sum_{n=1}^{N} \sum_{m=1}^{F_{YX}^2} (g_{origin}(a_{n,m}) - g(a_{n,m}))^2 \qquad (22)$$

where $g_{origin}(a_{n,m})$ is the gray value in the origin fine-resolution PAN image and $g(a_{n,m})$ is the gray value in the interpolated fine-resolution PAN image.

V. EXPERIMENTAL RESULTS

A. Degraded QuickBird Image

1) Data Description: A QuickBird image of Wuhan, Hubei Province, China, was used to test the performance of the proposed model. The experiment was conducted in areas of 20×20 pixels of 2.4-m spatial resolution MS bands (near-infrared, red, green, and blue) and 80×80 pixels of a 0.6-m spatial resolution PAN band. The MS image was degraded to a 4.8-m spatial resolution MS image, and the PAN image was degraded to a 1.2-m spatial resolution PAN image as the data source ($F_{YX} = 8, F_{ZX} = 2$) using a pixel aggregate function [see Fig. 4(a) and (b)] [46]. This simulation method ensured that there was no image registration error between the reference map and the resultant SR land cover map [31], [32]. The 0.6-m PAN image was manually digitized to represent the reference land cover map [see Fig. 4(c)]. Three land cover classes are present
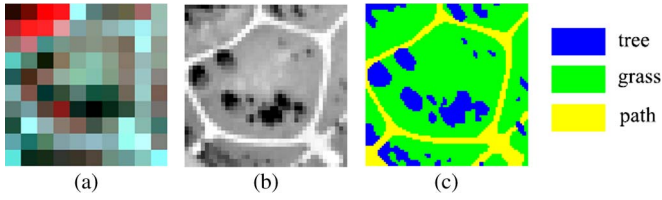
Fig. 4. (a) 4.8-m degraded QuickBird MS image (band 4-3-2) (b) 1.2-m degraded QuickBird PAN image (c) 0.6-m reference land cover map.

in the images: grass, tree, and path. The endmember signatures were selected from the degraded MS and PAN images.

2) Model Description: The performance of the SA_SSMSRM model was compared with a hard classification model and different SRM models. In this paper, a maximum likelihood classifier (MLC) was used to generate a hard classification map based on an MS image. A traditional SRM solely using fraction images extracted from the MS image as input was adopted. First, a constraint linear unmixing model (CLUM) was used to unmix pixels. Then, a PSA was used to allocate the subpixels (CLUM_PSA) [11], [12]. The proposed SA_SSMSRM was also compared with O_SSMSRM with a fixed nonadaptive smoothing parameter that was applied to both MS and PAN images.

The performances of different SRM models were affected by their parameters. A set of parameters was tested to fully understand the influences of these parameters on SRM results. For CLUM_PSA, the neighborhood window size W was set as 5 [35]. For both O_SSMSRM and SA_SSMSRM, W was set as 3, 5, 7, and 9, respectively. The O_SSMSRM smoothing parameter λ was set from 10 (a relative small value which led to insufficient smoothing of the SR map) to 2000 (a relative large value which led to oversmoothing of the SR map) with an interval of 10. For SA_SSMSRM, the smoothing parameter λ_0 ranged from 0.1 to 0.5 with an interval of 0.1. The process of determining the appropriate value of the nonlinear parameter σ in SA_SSMSRM is complex. Generally, the value of σ should not be beyond the interpolated PAN pixel photometric distance of class boundaries. Otherwise, the smoothing parameter values of subpixels located in homogeneous regions and class boundaries are approximate. However, the interpolated PAN pixel photometric distances between class boundaries in the image are spatially variable, making it complex to determine the value of σ properly. An index, called the average PAN pixel photometric distance of endmember signatures (I_{APPPD}), was used to determine the value of σ in this paper. I_{APPPD} adopts the average photometric distance between all different pairs of endmember signatures in the PAN image as an indicator of the interpolated PAN pixel photometric distance of class boundaries

$$I_{APPPD} = \frac{\left(\sum_{\alpha=1}^{c-1} \sum_{\beta=\alpha+1}^{c} \left| S_{PAN(C\alpha)} - S_{PAN(C\beta)} \right| \right)}{\frac{c \cdot (c-1)}{2}} \quad (23)$$

where $S_{PAN(C\alpha)}$ and $S_{PAN(C\beta)}$ represent the spectral signatures of land covers α and β in the PAN image. The nonlinear

parameter σ was set as $I_{APPPD}/20$, $I_{APPPD}/10$, $I_{APPPD}/5$, $I_{APPPD}/4$, $I_{APPPD}/3$, $I_{APPPD}/2$, and I_{APPPD}, respectively. SRM was run ten times for each combination of the aforementioned parameters. The average OA value for O_SSMSRM, which was averaged from ten repetitive experiments with the same model parameters of W and λ, and the average OA value for SA_SSMSRM, which was averaged from ten repetitive experiments with the same model parameters of W, λ_0, and σ and the same PAN image interpolation algorithms, were calculated for comparison.

3) Results: All models were tested on an Intel Core 2 Processor 2.66-GHz Duo CPU with 1.98-GB RAM using MATLAB version 7.3. The iteration numbers were 120 for both O_SSMSRM and SA_SSMSRM with the same parameters in simulated annealing optimization. The running time was about 35 s for CLUM_PSA, 120 s for O_SSMSRM, and 210 s for SA_SSMSRM. The OA values for MLC and CLUM_PSA were very low. For MLC, the OA value was 0.6753, and the fraction RMSE was 0.4612. For CLUM_PSA, the OA value was 0.6413, and the fraction RMSE was 0.4093. The highest average OA values denoted as OA*, which were derived from the average OA values with the same value of W and different values of λ for O_SSMSRM or derived from the average OA values with the same value of W and σ and the same PAN image interpolation algorithm and different values of λ_0 for SA_SSMSRM, are shown in Fig. 5. For SSMSRM, the OA* value increased to higher than 0.8, and the fraction RMSE values decreased to lower than 0.3 (see Fig. 5). This improvement showed the advantage of incorporating the PAN image in an SRM model. The OA* value for O_SSMSRM varied with the window size W. When $W = 3$, only eight subpixels were included in the neighborhood, and the spatial smoothing effect was not obvious. When $W = 9$, there were many neighboring subpixels included in the neighborhood, which may probably lead to a significant oversmoothing effect on SR maps produced by O_SSMSRM. Results showed that O_SSMSRM can generate an SR map with OA* of 0.8514 when $W = 5$ with the corresponding fraction RMSE of 0.2810.

The PAN image interpolation algorithms, the window size W, and the nonlinear parameter σ played a combined role in the optimization of OA* for SA_SSMSRM. The OA* values were low when $W = 3$ for different PAN image interpolation algorithms because the spatial smoothing effect was not obvious. By contrast, the OA* values were similar and relative higher when W was larger than 3 with different interpolated PAN images, with the variation of σ. The pixel values of the nearest-neighbor interpolated PAN image were piecewise constant [see Fig. 6(a)]. The subpixels in the same PAN pixel shared the same pixel value in the interpolated image, whereas the subpixels in different PAN pixels had different pixel values in most cases. As a result, the SA_SSMSRM smoothing parameter values for neighboring subpixels, which were calculated based on the interpolated PAN image pixels, were discontinuous. The OA* value for SA_SSMSRM with the nearest-neighbor interpolated PAN image was 0.8741 ($W = 9$, $\sigma = I_{APPPD}/10$, and the corresponding fraction RMSE was 0.2507). By contrast, the bilinear and bicubic interpolated PAN images were smoother [see Fig. 6(b) and (c)]. The MSE
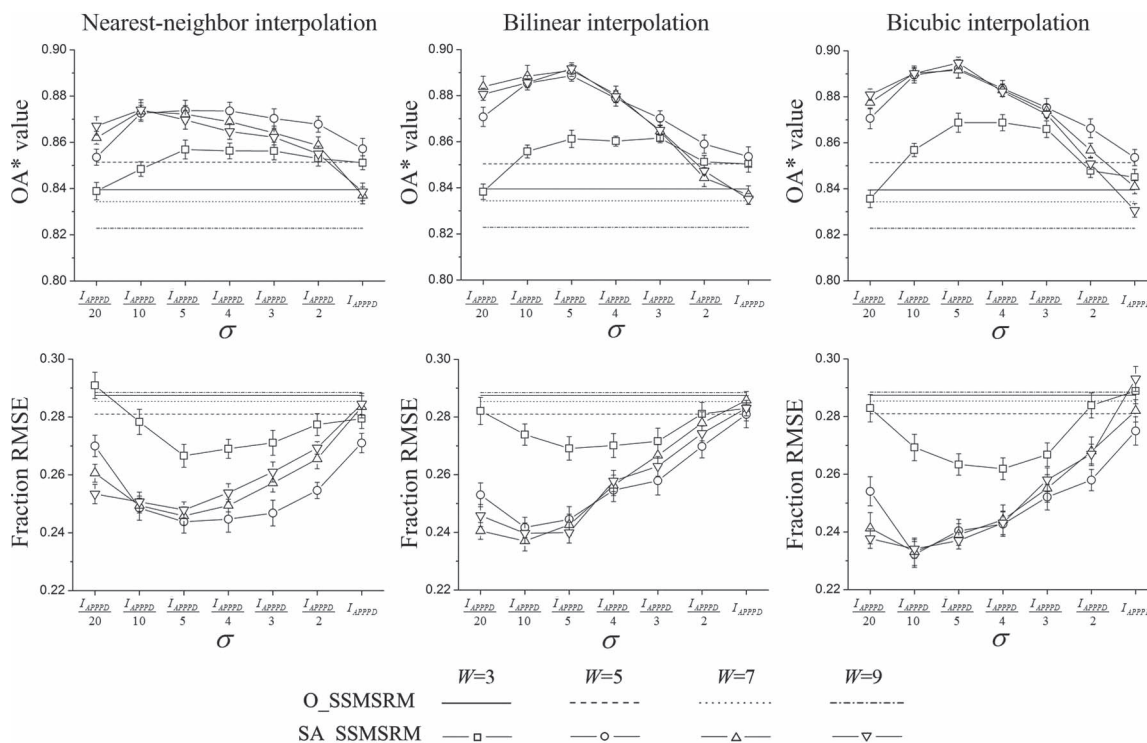
Fig. 5. OA* values and the corresponding fraction RMSE values for O_SSMSRM and SA_SSMSRM with the variation of PAN image interpolation algorithms, window size W, and nonlinear parameter σ for QuickBird image. Error bars represent standard deviation of the OA* values and fraction RMSE values.
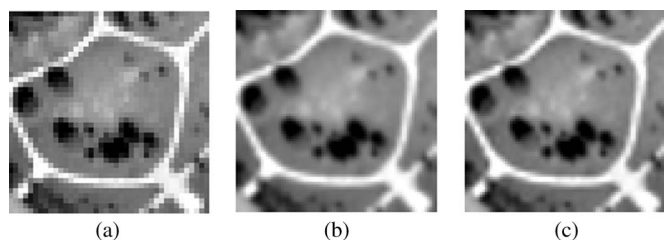

Fig. 6. Interpolated QuickBird PAN image produced by (a) nearest-neighbor interpolation, (b) bilinear interpolation, and (c) bicubic interpolation.

values of bilinear and bicubic interpolated PAN images were 182.16 and 102.44, respectively, lower than that of the nearest-neighbor interpolation (MSE = 264.56). The OA* value for SA_SSMSRM with the bilinear interpolated PAN image was 0.8917 ($W = 9$, $\sigma = I_{APPPD}/5$, and the corresponding fraction RMSE was 0.2399), and the OA* value for SA_SSMSRM with the bicubic interpolated PAN image was 0.8947 ($W = 9$, $\sigma = I_{APPPD}/5$, and the corresponding fraction RMSE was 0.2370).

The OA* value and fraction RMSE values for SA_SSMSRM were related to σ. For different values of W and PAN image interpolation algorithms, the OA* value was obtained when $\sigma = I_{APPPD}/10$ or $\sigma = I_{APPPD}/5$. When σ was small, the smoothing parameter values for subpixels with large PAN pixel photometric distances were probably oversuppressed. When σ was extremely large, the smoothing parameter values for subpixels with different PAN pixel photometric distances were almost equal, and SA_SSMSRM generated similar SR maps as O_SSMSRM.
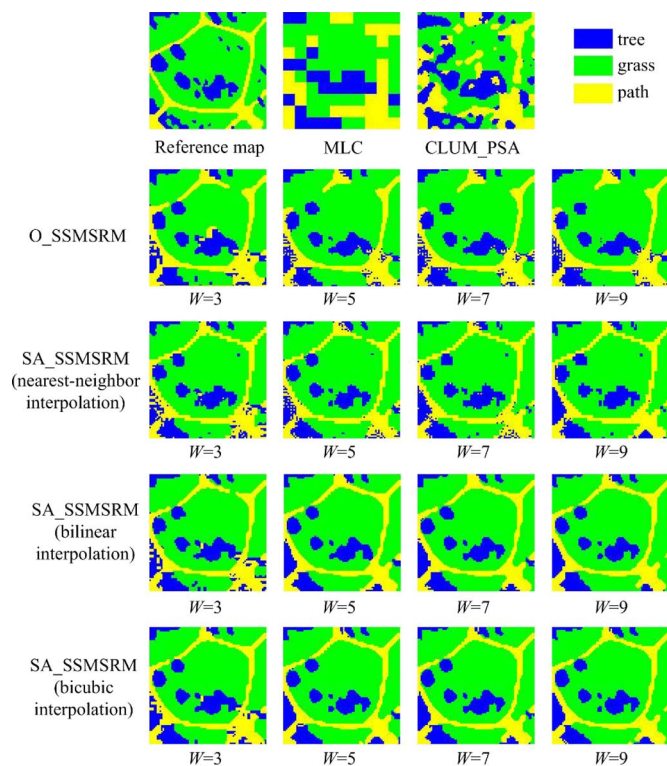

Fig. 7. Reference land cover map, hard classification map produced by MLC, and SR maps produced by different SRM models with different parameters for QuickBird image.

The hard classification map generated by MLC and the SR maps generated by different SRM models in terms of OA* are shown in Fig. 7. The hard classification map was generated

TABLE II
SMOOTHING PARAMETER VALUES FOR O_SSMSRM AND SA_SSMSRM
CORRESPONDING TO OA* FOR QUICKBIRD IMAGE

		$W=3$	$W=5$	$W=7$	$W=9$
O_SSMSRM (λ)		1650	1190	860	640
SA_SSMSRM (λ_0)	nearest-neighbor interpolation	0.2	0.2	0.3	0.5
	bilinear interpolation	0.2	0.3	0.2	0.3
	bicubic interpolation	0.3	0.2	0.4	0.3

Fig. 8. (a) 8-m degraded IKONOS MS image (band 4-3-2). (b) 2-m degraded IKONOS PAN image. (c) 1-m reference land cover map.

at the pixel scale, and the class boundaries were rough. In the SR map generated by CLUM_PSA, small structure details were lost due to the low spatial resolution of MS pixels. This problem became severer when the path object was smaller than the spatial resolution of the MS pixel. Numerous parts of the SR map generated by O_SSMSRM were rough along the class boundaries when $W = 3$. Jagged boundaries and several speckle artifacts remained with increased W, and the path was separated into discrete units which attribute to oversmoothing. Therefore, adopting a fixed smoothing parameter in SSMSRM cannot reconstruct homogeneous regions and class boundaries simultaneously.

By contrast, the SR maps generated by SA_SSMSRM were obviously similar to the reference map. Most path objects were connected, and speckle artifacts were almost eliminated. The PAN image pixel values were piecewise constant after the nearest-neighbor interpolation [see Fig. 6(a)]. Consequently, the smoothing parameter values for neighboring subpixels were piecewise constant and discontinuous, and the class boundaries were irregular and rough. The interpolated PAN image pixel values were continuous after bilinear and bicubic interpolations [see Fig. 6(b) and (c)], and the class boundaries in the corresponding SR maps were smoothed. The improvement was obvious by identifying the path smaller than the MS spatial resolution. The local variance of PAN pixel values is usually high for small objects, and the PAN pixel photometric distances between subpixels located on class boundaries are more distant. The objects smaller than the MS spatial resolution, which were smoothed and clustered into large objects in SR maps produced by O_SSMSRM, were better preserved in SR maps produced by SA_SSMSRM.

The smoothing parameter values for O_SSMSRM and SA_SSMSRM corresponding to OA* for the QuickBird image are listed in Table II. The range of the optimal smoothing parameter value for O_SSMSRM was much larger than that for SA_SSMSRM. Consequently, a longer time was required to find the optimal smoothing parameter value, which hindered the application of O_SSMSRM to some extent. By contrast, the optimal smoothing parameter value for SA_SSMSRM was easier to determine due to the injection of the adaptive coefficients in prior and spectral terms.

B. Degraded IKONOS Image

1) Data and Model Description: An IKONOS image of Dujiangyan, Sichuan Province, China, was also adopted to
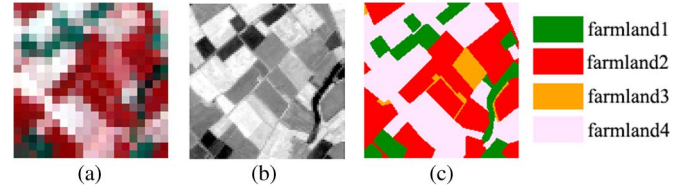
compare the performance of different models. The experiment was implemented in areas of 40×40 pixels of 4-m spatial resolution MS bands (near-infrared, red, green, and blue) and 160×160 pixels of a 1-m spatial resolution PAN band. The MS image was degraded to an 8-m MS image, and the PAN image was degraded to a 2-m PAN image as the data source ($F_{YX} = 8, F_{ZX} = 2$) using the pixel aggregate function [see Fig. 8(a) and (b)]. The PAN image was manually digitized to represent the reference land cover map [see Fig. 8(c)]. Four kinds of farmlands were present in the images. The endmember signatures were selected from the degraded MS and PAN images. MLC, CLUM_PSA, O_SSMSRM, and SA_SSMSRM were compared. The parameters for different SRM models were set the same as those used in the QuickBird image experiment. SRM was run ten times for each combination of the parameters.

2) Results: The running time was about 190 s for CLUM_PSA, 630 s for O_SSMSRM, and 1100 s for SA_SSMSRM. For MLC, the OA value was 0.8204, and the fraction RMSE value was 0.2971. For CLUM_PSA, the OA value was 0.7841, and the fraction RMSE was 0.2946. For O_SSMSRM and SA_SSMSRM using both MS and PAN images as input, the OA* values increased to higher than 0.88, and the fraction RMSE values decreased to lower than 0.22 (see Fig. 9). For O_SSMSRM, the OA* value was 0.9366, and the lowest fraction RMSE was 0.1612 when $W = 5$. The OA* value for SA_SSMSRM varied with PAN image interpolation algorithms, window size W, and nonlinear parameter σ. The OA* value for SA_SSMSRM with the bilinear and bicubic interpolated PAN images was higher than that using the nearest-neighbor interpolated PAN image because the nearest-neighbor interpolated PAN image was piecewise constant [see Fig. 10(a)–(c)]. The MSE value of the nearest-neighbor interpolated PAN image was 531.01, higher than the MSE values of the bilinear interpolated (MSE = 442.30) and bicubic interpolated (MSE = 346.22) PAN images. The OA* value for SA_SSMSRM was 0.9531 (bicubic interpolation, $W = 7$, $\sigma = I_{APPPD}/4$, and the corresponding fraction RMSE was 0.1421), which was 0.0165 higher than that of O_SSMSRM.

The hard classification map and the SR maps generated from different models are shown in Fig. 11. The hard classification map was generated with jagged boundaries because of the low MS image spatial resolution. There were many speckle artifacts in the SR map produced by CLUM_PSA due to MS pixel spectral unmixing error. For instance, assuming that the spectral unmixing error for a pure MS pixel is 18.75%, there will be $F_{YX}^2 \times 0.1875 = 12$ subpixels labeled as wrong classes.
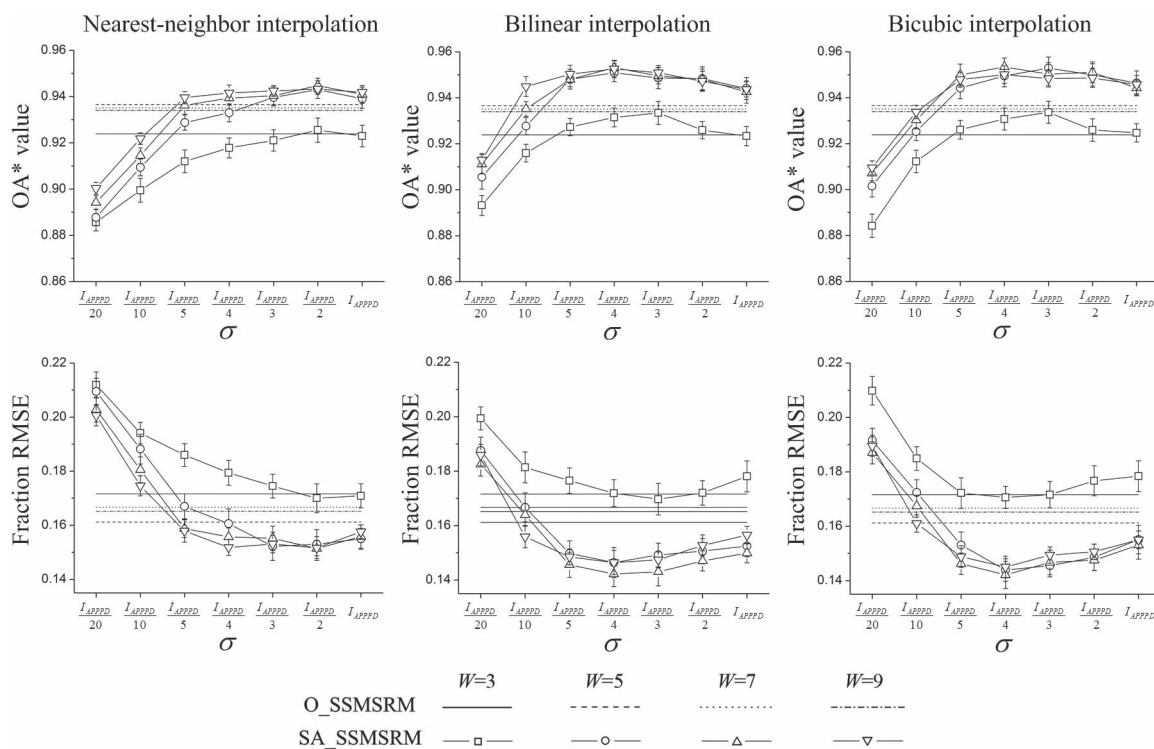
Fig. 9. OA* values and the corresponding fraction RMSE values for O_SSMSRM and SA_SSMSRM with the variation of PAN image interpolation algorithms, window size W, and the nonlinear parameter σ for IKONOS image. Error bars represent standard deviation of the OA* values and fraction RMSE values.
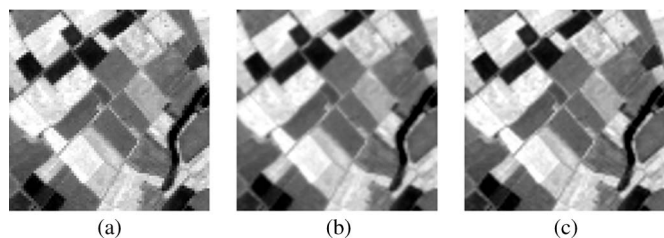

Fig. 10. Interpolated IKONOS PAN image produced by (a) nearest-neighbor interpolation, (b) bilinear interpolation, and (c) bicubic interpolation.

These 12 subpixels exist as speckle artifacts in the CLUM_PSA result. Additionally, the path which was smaller than the spatial resolution of the MS pixel (located in the middle of the scene) was not mapped by CLUM_PSA. By contrast, a part of the path was mapped by adding a fine resolution of the PAN image as input. Most speckle artifacts were eliminated due to the spatial smoothing effect of SSMSRM. For O_SSMSRM, the path was partly mapped when W was not larger than 5. The path was eliminated, and the corners of objects were rounded when W was larger than 5 due to the oversmoothing effect. By contrast, a larger part of the path and many land cover object corners were retained in the SA_SSMSRM maps. Parts of class boundaries were roughly produced by SA_SSMSRM with the nearest-neighbor interpolated PAN image, whereas class boundaries were smoothly produced by SA_SSMSRM with the bilinear and bicubic interpolated PAN images. Moreover, the optimal smoothing parameter value for SA_SSMSRM was easier to determine compared with that for O_SSMSRM (see Table III), showing the advantage of the proposed model.
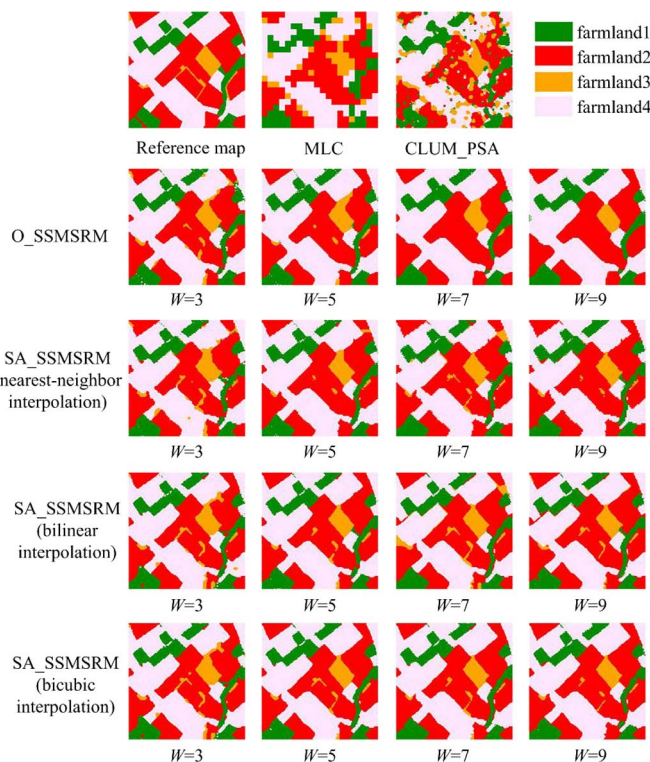

Fig. 11. Reference land cover map, hard classification map produced by MLC, and SR maps produced by different SRM models with different parameters for IKONOS image.

From the aforementioned experimental results using two degraded images, the performances of SA_SSMSRM and O_SSMSRM were affected by many factors. First, the

		$W=3$	$W=5$	$W=7$	$W=9$
O_SSMSRM (λ)		1340	900	620	440
SA_SSMSRM (λ_0)	nearest-neighbor interpolation	0.2	0.2	0.2	0.4
	bilinear interpolation	0.2	0.3	0.4	0.3
	bicubic interpolation	0.2	0.2	0.4	0.4

accuracies in the IKONOS experiment were higher than those in the QuickBird experiment for both SA_SSMSRM and O_SSMSRM. This is because the performance of SSMSRM is affected by land cover class spectral separability [24]. Class spectral separability plays a role in SSMSRM that is similar to the signal-to-noise ratio in signal processing, and lower class spectral separability will lead SSMSRM to confuse between classes. The average Bhattacharyya distance [24], which measures the average class spectral separability between different pairs of classes, was used in this paper. The average Bhattacharyya distance was 6.048 for the QuickBird MS image, lower than that of 16.343 for the IKONOS MS image; the average Bhattacharyya distance was 5.870 for the QuickBird PAN image, lower than that of 6.261 for the IKONOS PAN image. Second, the improvement of SA_SSMSRM versus O_SSMSRM was more obvious in the QuickBird experiment than in the IKONOS experiment. This is because the greatest improvement of SA_SSMSRM was reconstructing the path objects that were smaller than the spatial resolution of MS image pixels, and there were more path objects with small size in the QuickBird image than in the IKONOS image. In summary, the proposed SA_SSMSRM can perform better when the image provides high class spectral separability between land cover classes and can show its greatest improvement compared with other SRM models when the image contains many objects that are smaller than the MS image pixel.

C. Real ALOS Image

1) Data and Model Description: An investigation on real ALOS remotely sensed images was conducted. A subset centered on an airport in Haneda, Japan, acquired on March 1, 2007, was used as the data source. The subset covered an MS image (100×100 pixels) acquired by the Advanced Visible and Near Infrared Radiometer type-2 (with the spatial resolution of 10 m and four bands of near-infrared, red, green, and blue) and a PAN image (400×400 pixels) acquired by the Panchromatic Remote-sensing Instrument for Stereo Mapping (with the spatial resolution of 2.5 m), which are shown in Fig. 12(a) and (b) ($F_{YZ} = 4$). A Google Earth image acquired on February 12, 2007 with the spatial resolution higher than that of the ALOS PAN image was manually digitalized as the reference map [see Fig. 12(c)]. The root-mean-square error of image registration for MS and PAN images and for the PAN and Google Earth image was less than 1 pixel of the PAN image. Each
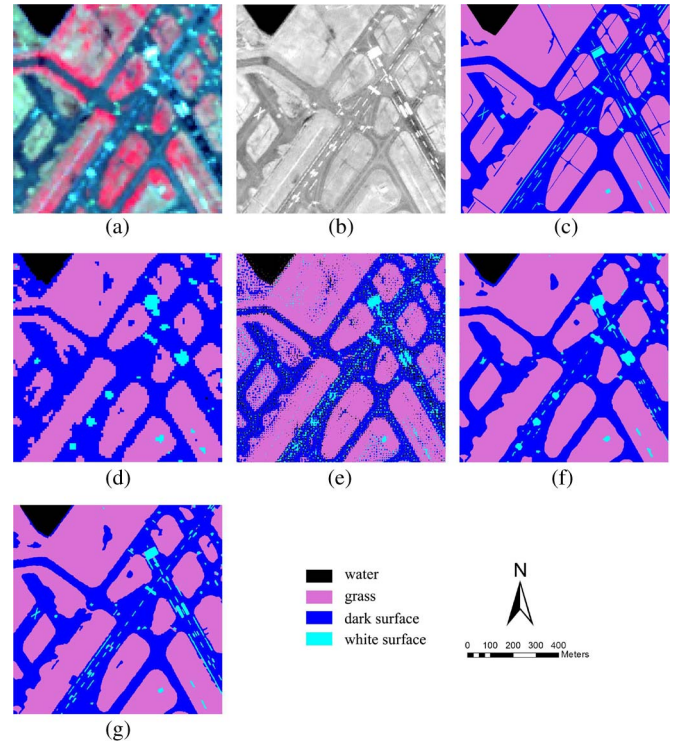

Fig. 12. (a) 10-m ALOS MS image (band 4-3-2). (b) 2.5-m ALOS PAN image. (c) 1.25-m reference land cover map. (d) Hard classification map produced by MLC. (e) SR map produced by CLUM_PSA. (f) SR map produced by O_SSMSRM according to the highest OA value ($\lambda = 7$). (g) SR map produced by SA_SSMSRM.

PAN image pixel contained 4 fine-resolution reference image pixels ($F_{ZX} = 2$). Four land cover classes (water, grass, dark surface, and white surface) were included. The endmember signatures were selected from the MS and PAN images directly. MLC, CLUM_PSA, and O_SSMSRM were compared with SA_SSMSRM. For CLUM_PSA, the neighborhood window size W was set as 5. For O_SSMSRM, W was set as 5, and λ ranged from 1 to 20 with an interval of 1. For SA_SSMSRM, bilinear interpolation was used for PAN image interpolation. SA_SSMSRM parameters were as follows: $W = 7$, $\lambda_0 = 0.3$, and $\sigma = I_{APPPD}/10$.

2) Results: The maps generated by different models are shown in Fig. 12. In the hard classification map, the class boundaries were rough [see Fig. 12(d)]. Many small white surface objects (smaller than an MS pixel) were eliminated. In the SR map generated by CLUM_PSA, many speckle artifacts existed due to the pixel spectral unmixing error [see Fig. 12(e)]. Most of the speckle artifacts were eliminated due to the spatial smoothing effect of O_SSMSRM [see Fig. 12(f)]. Some small white surface objects were mapped in the SR result due to the injection of the PAN image. However, the spatial details of many white surface objects were lost. Many connected white surface objects were incorrectly separated, and some adjacent objects were incorrectly combined. A great improvement of small structure details was found in the SA_SSMSRM map in which the spatial details of small objects matched those in the reference map much better [see Fig. 12(g)]. The accuracy statistics of different models are listed in Table IV.

TABLE IV
ACCURACY STATISTICS OF DIFFERENT MODELS

	MLC	CLUM_PSA	O_SSMSRM	SA_SSMSRM
Overall accuracy	0.8570	0.8247	0.9039	0.9104
Fraction RMSE	0.2298	0.2705	0.1844	0.1749

Although the improvement of accuracy was not very obvious because there were many pure pixels in the image, the SA_SSMSRM model can generate SR maps with higher OA value and lower fraction RMSE value compared with other models.

VI. CONCLUSION

A spatially adaptive SRM model is proposed in this paper. The proposed SA_SSMSRM model incorporates both MS and PAN images as input and can be applied directly to remotely sensed images. Similar to previous SRM models, the proposed model uses PAN image pixel values as the spectral constraint. In addition, the proposed model also uses the PAN image pixel photometric distance to identify homogeneous regions of objects and class boundaries. The homogeneous regions in the PAN images are characterized by the photometric similarity, whereas class boundaries are characterized by photometric dissimilarity. Spatially adaptive smoothing parameters are designed based on the similarity of PAN image pixel values between the central subpixel and its neighboring subpixels. The SA_SSMSRM model can smooth homogeneous regions and preserve class boundaries simultaneously. Moreover, the value of the appropriate smoothing parameter is affected by the data ranges of the prior and spectral terms. In the proposed model, the prior and spectral terms are divided by two adaptive coefficients which are calculated according to the statistical characteristics of the data ranges of the prior and spectral terms when optimizing the model.

Both degraded and real remotely sensed images were used in experiments. The hard classification map generated land cover maps with jagged and rough boundaries. The SRM model, which first unmixed MS image pixel spectral term and then allocated the subpixels based on the fraction images, generated SR maps with many speckle artifacts due to pixel spectral unmixing error, and the object spatial details within the MS pixel were not mapped because of the coarse spatial resolution of the MS image. The SSMSRM model using MS and PAN images but with a fixed smoothing parameter could not smooth the homogeneous region and preserve the class boundary simultaneously, and speckle artifacts and oversmoothed class boundaries were often found in the SR map. By contrast, the SA_SSMSRM model smoothed the homogeneous region and preserved class boundaries simultaneously. The speckle artifacts were mostly eliminated, and the spatial details of land cover objects were preserved. Accuracy statistics showed that SA_SSMSRM generated SR maps with higher OA and lower fraction RMSE. Moreover, the range of the optimal smoothing parameter value of SSMSRM with a fixed smoothing parameter

value was much larger than that of SA_SSMSRM. The appropriate value of the smoothing parameter in SA_SSMSRM can be easily found, making the application of the proposed model more convenient. The experiment with the real remotely sensed image suggested that the proposed model requires accurate geometric registration between pixels of the MS and PAN images.

The application of SA_SSMSRM was affected by the input image and model parameters. First, SA_SSMSRM can perform better when the image provides high class spectral separability between land cover classes, and it shows its greatest improvement compared with other SRM models when the image contains many objects that are smaller than the MS image pixel. Second, the shadow pixels become more prominent in the PAN image as the spatial resolution increases. The shadow can be classified into a separate class in SA_SSMSRM. Finally, the performance of SA_SSMSRM was affected by model parameters. The nearest-neighbor interpolated PAN image was piecewise constant. In this way, the smoothing parameter values for neighboring subpixels were discontinuous, and the class boundaries were rough in the SR map. Bilinear and bicubic interpolations generated interpolated PAN images that were continuous in values, and the corresponding SR map had smoothed class boundaries with high OA. The window size W represented the number of neighboring subpixels. When $W = 3$, only 8 subpixels were used for spatial smoothing, and speckle artifacts were more likely to be found in the processed SR map. The window sizes of 5, 7, and 9 were recommended to eliminate speckle artifacts. The optimal value of the smoothing parameter λ_0 was not affected by the spectral range of MS and PAN images. The λ_0 was recommended to be 0.2–0.4 for various remotely sensed sensors. The appropriate value of the nonlinear parameters σ varied with different PAN images. Generally, the value of σ should not be set beyond the pixel photometric distance between class boundaries in interpolated PAN images so that the smoothing parameter values are not approximate for subpixels located in homogeneous regions and class boundaries. In this paper, the average PAN pixel photometric distance of the endmember signature index was proposed to facilitate the setting of σ appropriately. Experiments showed that the SA_SSMSRM generated a high-accuracy SR map when σ ranged from one-tenth to half of the average PAN pixel photometric distance of the endmember signature index value.

The integration of different remotely sensed data (including MS image, PAN image, DEM, LIDAR, etc.) is an interesting task for providing more information in SRM. An important issue is what kind of information is to be used for SRM. For instance, a PAN image provides both spectral information and texture information of land cover objects that are useful for SRM. Furthermore, how to use the information provided by the data to conduct an SRM model with less and easy-to-determine model parameters is important when applying SRM into practical applications, particularly when directly applying SRM to remotely sensed images instead of assuming that the fraction images are ideally acquired without errors. A comprehensive study of more effectively utilizing the multisource data for SRM is required in the future.

REFERENCES

[1] P. M. Atkinson, "Mapping sub-pixel boundaries from remotely sensed images," in *Innovations in GIS*. New York, NY, USA: Taylor & Francis, 1997, pp. 166–180.

[2] P. M. Atkinson, "Issues of uncertainty in super-resolution mapping and their implications for the design of an inter-comparison study," *Int. J. Remote Sens.*, vol. 30, no. 20, pp. 5293–5308, Oct. 2009.

[3] A. J. Tatem, H. G. Lewis, P. M. Atkinson, and M. S. Nixon, "Increasing the spatial resolution of agricultural land cover maps using a Hopfield neural network," *Int. J. Geograph. Inf. Sci.*, vol. 17, no. 7, pp. 647–672, Oct./Nov. 2003.

[4] M. W. Thornton, P. M. Atkinson, and D. A. Holland, "Sub-pixel mapping of rural land cover objects from fine spatial resolution satellite sensor imagery using super-resolution swapping," *Int. J. Remote Sens.*, vol. 27, no. 3, pp. 473–491, Feb. 2006.

[5] G. M. Foody, A. M. Muslim, and P. M. Atkinson, "Super-resolution mapping of the waterline from remotely sensed data," *Int. J. Remote Sens.*, vol. 26, no. 24, pp. 5381–5392, Dec. 2005.

[6] F. Ling, F. Xiao, Y. Du, H. Xue, and X. Ren, "Waterline mapping at the subpixel scale from remote sensing imagery with high-resolution digital elevation models," *Int. J. Remote Sens.*, vol. 29, no. 6, pp. 1809–1815, Mar. 2008.

[7] F. Ling, X. Li, F. Xiao, S. Fang, and Y. Du, "Object-based sub-pixel mapping of buildings incorporating the prior shape information from remotely sensed imagery," *Int. J. Appl. Earth Observ. Geoinf.*, vol. 18, pp. 283–292, Aug. 2012.

[8] J. P. Ardila, V. A. Tolpekin, W. Bijker, and A. Stein, "Markov-random-field-based super-resolution mapping for identification of urban trees in VHR images," *ISPRS J. Photogramm. Remote Sens.*, vol. 66, no. 6, pp. 762–775, Nov. 2011.

[9] F. Ling, W. Li, Y. Du, and X. Li, "Land cover change mapping at the subpixel scale with different spatial-resolution remotely sensed imagery," *IEEE Geosci. Remote Sens. Lett.*, vol. 8, no. 1, pp. 182–186, Jan. 2011.

[10] X. Li, Y. Du, F. Ling, S. Wu, and Q. Feng, "Using a sub-pixel mapping model to improve the accuracy of landscape pattern indices," *Ecological Indicators*, vol. 11, no. 5, pp. 1160–1170, Sep. 2011.

[11] P. M. Atkinson, "Sub-pixel target mapping from soft-classified, remotely sensed imagery," *Photogramm. Eng. Remote Sens.*, vol. 71, no. 7, pp. 839–846, Jul. 2005.

[12] Y. Makido, A. Shortridge, and J. P. Messina, "Assessing alternatives for modeling the spatial distribution of multiple land-cover classes at sub-pixel scales," *Photogramm. Eng. Remote Sens.*, vol. 73, no. 8, pp. 935–943, Aug. 2007.

[13] F. Ling, Y. Du, F. Xiao, H. Xue, and S. Wu, "Super-resolution land-cover mapping using multiple sub-pixel shifted remotely sensed images," *Int. J. Remote Sens.*, vol. 31, no. 19, pp. 5023–5040, Oct. 2010.

[14] A. J. Tatem, H. G. Lewis, P. M. Atkinson, and M. S. Nixon, "Super-resolution target identification from remotely sensed images using a Hopfield neural network," *IEEE Trans. Geosci. Remote Sens.*, vol. 39, no. 4, pp. 781–796, Apr. 2001.

[15] J. Verhoeye and R. De Wulf, "Land cover mapping at sub-pixel scales using linear optimization techniques," *Remote Sens. Environ.*, vol. 79, no. 1, pp. 96–104, Jan. 2002.

[16] F. Ling, X. Li, Y. Du, and F. Xiao, "Sub-pixel mapping of remotely sensed imagery with hybrid intra- and inter-pixel dependence," *Int. J. Remote Sens.*, vol. 34, no. 1, pp. 341–357, Jan. 2013.

[17] Y. Ge, S. Li, and V. C. Lakhan, "Development and testing of a subpixel mapping algorithm," *IEEE Trans. Geosci. Remote Sens.*, vol. 47, no. 7, pp. 2155–2164, Jul. 2009.

[18] K. C. Mertens, B. De Baets, L. P. C. Verbeke, and R. R. De Wulf, "A sub-pixel mapping algorithm based on sub-pixel/pixel spatial attraction models," *Int. J. Remote Sens.*, vol. 27, no. 15, pp. 3293–3310, Aug. 2006.

[19] Z. Shen, J. Qi, and K. Wang, "Modification of pixel-swapping algorithm with initialization from a sub-pixel/pixel spatial attraction model," *Photogramm. Eng. Remote Sens.*, vol. 75, no. 5, pp. 557–567, May 2009.

[20] K. C. Mertens, L. P. C. Verbeke, E. I. Ducheyne, and R. R. De Wulf, "Using genetic algorithms in sub-pixel mapping," *Int. J. Remote Sens.*, vol. 24, no. 21, pp. 4241–4247, Jan. 2003.

[21] Q. M. Wang, L. G. Wang, and D. F. Liu, "Particle swarm optimization-based sub-pixel mapping for remote-sensing imagery," *Int. J. Remote Sens.*, vol. 33, no. 20, pp. 6480–6496, Oct. 2012.

[22] F. Ling, Y. Du, X. Li, W. Li, F. Xiao, and Y. Zhang, "Interpolation-based super-resolution land cover mapping," *Remote Sens. Lett.*, vol. 4, no. 7, pp. 629–638, Jul. 2013.

[23] T. Kasetkasem, M. K. Arora, and P. K. Varshney, "Super-resolution land cover mapping using a Markov random field based approach," *Remote Sens. Environ.*, vol. 96, no. 3/4, pp. 302–314, Jun. 2005.

[24] V. A. Tolpekin and A. Stein, "Quantification of the effects of land-cover-class spectral separability on the accuracy of Markov-random-field-based superresolution mapping," *IEEE Trans. Geosci. Remote Sens.*, vol. 47, no. 9, pp. 3283–3297, Sep. 2009.

[25] F. Ling, Y. Du, F. Xiao, and X. Li, "Subpixel land cover mapping by integrating spectral and spatial information of remotely sensed imagery," *IEEE Geosci. Remote Sens. Lett.*, vol. 9, no. 3, pp. 408–412, May 2012.

[26] X. Li, F. Ling, and Y. Du, "Super-resolution mapping based on the supervised fuzzy c-means approach," *Remote Sens. Lett.*, vol. 3, no. 6, pp. 501–510, Nov. 2012.

[27] P. Aplin and P. M. Atkinson, "Sub-pixel land cover mapping for per-field classification," *Int. J. Remote Sens.*, vol. 22, no. 14, pp. 2853–2858, Jan. 2001.

[28] M. Q. Nguyen, P. M. Atkinson, and H. G. Lewis, "Superresolution mapping using a Hopfield neural network with LIDAR data," *IEEE Geosci. Remote Sens. Lett.*, vol. 2, no. 3, pp. 366–370, Jul. 2005.

[29] W. Sun, V. Heidt, P. Gong, and G. Xu, "Information fusion for rural land-use classification with high-resolution satellite imagery," *IEEE Trans. Geosci. Remote Sens.*, vol. 41, no. 4, pp. 883–890, Apr. 2003.

[30] M. Mueller, K. Segl, and H. Kaufmann, "Edge- and region-based segmentation technique for the extraction of large, man-made objects in high-resolution satellite imagery," *Pattern Recognit.*, vol. 37, no. 8, pp. 1619–1628, Aug. 2004.

[31] M. Q. Nguyen, P. M. Atkinson, and H. G. Lewis, "Superresolution mapping using a Hopfield neural network with fused images," *IEEE Trans. Geosci. Remote Sens.*, vol. 44, no. 3, pp. 736–749, Mar. 2006.

[32] Q. M. Nguyen, P. M. Atkinson, and H. G. Lewis, "Super-resolution mapping using Hopfield neural network with panchromatic imagery," *Int. J. Remote Sens.*, vol. 32, no. 21, pp. 6149–6176, Nov. 2011.

[33] X. Li, Y. Du, and F. Ling, "Spatially adaptive smoothing parameter selection for Markov random field based sub-pixel mapping of remotely sensed images," *Int. J. Remote Sens.*, vol. 33, no. 24, pp. 7886–7901, Dec. 2012.

[34] X. Jia and J. A. Richards, "Managing the spectral-spatial mix in context classification using Markov random fields," *IEEE Geosci. Remote Sens. Lett.*, vol. 5, no. 2, pp. 311–314, Apr. 2008.

[35] Y. Makido and A. Shortridge, "Weighting function alternatives for a sub-pixel allocation model," *Photogramm. Eng. Remote Sens.*, vol. 73, no. 11, pp. 1233–1240, Nov. 2007.

[36] J. Li, J. M. Bioucas-Dias, and A. Plaza, "Spectral-spatial hyperspectral image segmentation using subspace multinomial logistic regression and Markov random fields," *IEEE Trans. Geosci. Remote Sens.*, vol. 50, no. 3, pp. 809–823, Mar. 2012.

[37] Y. Tarabalka, M. Fauvel, J. Chanussot, and J. A. Benediktsson, "SVM- and MRF-based method for accurate classification of hyperspectral images," *IEEE Geosci. Remote Sens. Lett.*, vol. 7, no. 4, pp. 736–740, Oct. 2010.

[38] A. C. Popescu and H. Farid, "Exposing digital forgeries in color filter array interpolated images," *IEEE Trans. Signal Process.*, vol. 53, no. 10, pp. 3948–3959, Oct. 2005.

[39] S. Farsiu, M. D. Robinson, M. Elad, and P. Milanfar, "Fast and robust multiframe super resolution," *IEEE Trans. Image Process.*, vol. 13, no. 10, pp. 1327–1344, Oct. 2004.

[40] C. Tomasi and R. Manduchi, "Bilateral filtering for gray and color images," in *Proc. IEEE Int. Conf. Comput. Vis.*, Bombay, India, Jan. 1998, pp. 839–846.

[41] B. Suman and P. Kumar, "A survey of simulated annealing as a tool for single and multiobjective optimization," *J. Oper. Res. Soc.*, vol. 57, no. 10, pp. 1143–1160, Oct. 2006.

[42] D. C. Heinz and C. I. Chang, "Fully constrained least squares linear spectral mixture analysis method for material quantification in hyperspectral imagery," *IEEE Trans. Geosci. Remote Sens.*, vol. 39, no. 3, pp. 529–545, Mar. 2001.

[43] S. Geman and D. Geman, "Stochastic relaxation, Gibbs distributions, and the Bayesian restoration of the images," *IEEE Trans. Pattern Anal. Mach. Intell.*, vol. PAMI-6, no. 6, pp. 721–741, Nov. 1984.

[44] R. G. Pontius, Jr. and M. Millones, "Death to Kappa: Birth of quantity disagreement and allocation disagreement for accuracy assessment," *Int. J. Remote Sens.*, vol. 32, no. 15, pp. 4407–4429, Aug. 2011.

[45] J. Jin, B. Wang, and L. Zhang, "A novel approach based on Fisher discriminant null space for decomposition of mixed pixels in hyperspectral imagery," *IEEE Geosci. Remote Sens. Lett.*, vol. 7, no. 4, pp. 699–703, Oct. 2010.

[46] L. Bian and R. Butler, "Comparing effects of aggregation methods on statistical and spatial properties of simulated spatial data," *Photogramm. Eng. Remote Sens.*, vol. 65, no. 1, pp. 73–84, Jan. 1999.
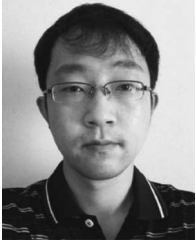
Xiaodong Li received the B.S. degree in geographic information system from the Chinese University of Geosciences, Wuhan, China, in 2006 and the M.S. and Ph.D. degrees in physical geography from the Institute of Geodesy and Geophysics, Chinese Academy of Sciences, Wuhan, in 2009 and 2012, respectively.

He is currently a Research Assistant with the Institute of Geodesy and Geophysics, Chinese Academy of Sciences. His research interest is the superresolution mapping of remotely sensed imagery.

Yun Du received the B.S. degree in geomorphology and quaternary geology from Nanjing University, Nanjing, China, in 1989, the M.S. degree in physical geography from the Institute of Geodesy and Geophysics, Chinese Academy of Sciences, Wuhan, China, in 1992, and the Ph.D. degree in historical geography from Wuhan University, Wuhan, in 1999.

He is currently a Professor with the Institute of Geodesy and Geophysics, Chinese Academy of Sciences. His research interests are remote sensing application and hydrology.

Feng Ling received the B.S. degree in geology and the M.S. degree in geophysical prospecting and information technology from the Chinese University of Geosciences, Wuhan, China, in 1999 and 2002, respectively, and the Ph.D. degree in system analysis and integration from the Huazhong University of Science and Technology, Wuhan, in 2006.

He is currently an Associate Professor with the Institute of Geodesy and Geophysics, Chinese Academy of Sciences, Wuhan. His research interests are superresolution mapping and uncertainty analysis of remotely sensed imagery.

Yihang Zhang is currently working toward the M.S. degree in physical geography at the Chinese Academy of Sciences, Wuhan, China.

His research interest is superresolution mapping of remotely sensed imagery.